A Congruent-Melting Mid-Infrared Nonlinear Optical Vanadate Exhibiting Strong Second-Harmonic Generation

Chao Wu,[†][a] Xingxing Jiang,[†][b] Longhua Li,[a] Zheshuai Lin,[b] Lin Lin,[a] Zhipeng Huang,[a] Mark G. Humphrey,[c] and Chi Zhang*[a]

[a] Dr. C. Wu, Dr. L. H. Li, L. Lin, Prof. Z. P. Huang, Prof. C. Zhang
China-Australia Joint Research Center for Functional Molecular Materials
School of Chemical Science and Engineering, Tongji University Shanghai 200092, China
E-mail: chizhang@tongji.edu.cn
[b] Dr. X. X. Jiang, Prof. Z. S. Lin
Technical Institute of Physics and Chemistry
Chinese Academy of Sciences, Beijing 100190, China
[c] Prof. M. G. Humphrey
Research School of Chemistry, Australian National University
Canberra, ACT 2601, Australia
[†] C. Wu and X. X. Jiang contributed equally to the work

Supporting information for this article is given via a link at the end of the document.

Abstract: Mid-infrared (mid-IR) nonlinear optical (NLO) materials are vital for the development of photonics research and state-of-the-art laser technology, but the study of these important optoelectronic materials is hindered by the competing requirements of optimized second-harmonic generation (SHG) coefficient d_{ij} and laser-induced damage threshold (LIDT), as well as the harsh synthetic conditions that are usually needed. Herein, we report the facile hydrothermal synthesis of a polar NLO vanadate $Cs_4V_8O_{22}$ (CVO) featuring a quasi-rigid honeycomb-layered structure with $[VO_4]$ and $[VO_5]$ polyhedra aligned parallel. CVO possesses a wide IR-transparent window, high LIDT, and congruent-melting behavior, and it displays amongst the largest phase-matchable SHG intensities for the metal vanadate family (12.0 × KH_2PO_4 @ 1064 nm and 2.2 × $AgGaS_2$ @ 2100 nm). First-principles calculations suggest that the exceptional SHG responses of CVO largely originate from virtual electronic transitions within the $[V_4O_{11}]_\infty$ layer, and that the excellent optical transmittance of CVO arises from the special characteristics of vibrational phonons resulting from the layered structure. These attributes suggest that CVO is an outstanding mid-IR NLO candidate material.

Introduction

Nonlinear optical (NLO) materials that can effect frequency conversion and the generation of coherent light have attracted considerable interest due to their potential for applications in laser and photonics technologies.[1,2] Significant progress has been achieved in the development of materials suitable for use in the deep-UV (DUV)-UV-Vis-Near-Infrared (NIR) regions, for which there are many efficient NLO oxide materials (e.g. β-BaB_2O_4 (BBO),[3a] LiB_3O_5 (LBO),[3b] CsB_3O_5 (CBO),[3c] and KH_2PO_4 (KDP)[3d]). In contrast, mid- and far-IR (MFIR) (> 3 μm) laser technology is still underexploited despite being the subject of intensive research over the past decade,[4] because the commercial IR NLO chalcogenide materials (e.g. the chalcopyrite crystals $AgGaS_2$,[5a] $AgGaSe_2$,[5b] and $ZnGeP_2$[5c]) exhibit significant drawbacks such as low laser-induced damage thresholds (LIDTs), deleterious two-photon absorption, and difficulty in crystal growth.[6] Lasers spanning the key atmospheric window (3−5 μm) are in particularly urgent demand for important practical applications such as laser guidance, telecommunication, remote sensing, and medical diagnostics,[7] and so the pursuit of IR NLO materials that can satisfy the crucial prerequisites (strong second-harmonic generation (SHG) effect, high LIDT, wide IR-transparent window, ease of single-crystal growth, congruent-melting crystals) remains a major challenge of contemporary materials research.[8]

Metal oxides have been of long-standing interest in the quest for high-performance NLO materials.[9] In comparison with non-oxides such as chalcogenides and pnictides,[10] traditional metal oxide IR NLO candidates (e.g. borates,[11] nitrates,[12] carbonates,[13] phosphates[14]) usually exhibit wider optical band gaps, higher LIDTs, and increased ease of single crystal growth, but their IR absorption edges do not reach 5 μm.[15] An emerging effective approach for developing mid-IR NLO materials is to introduce relatively heavy elements[16] such as d^0 transition metal (d^0-TM) cations (e.g. Ti^{4+}, V^{5+}, W^{6+}, Mo^{6+})[17] and stereochemically active lone-pair cations (e.g. Pb^{2+}, Bi^{3+}, Te^{4+}, I^{5+})[18] into metal oxides to extend IR absorption edges, relevant examples including M_2LiVO_4 (M = Rb, Cs, 4−5 × KDP),[19a] $Li_2K_4TiOGe_4O_{12}$ (2 × KDP),[19b] $Rb_4Li_2TiOGe_4O_{12}$ (2 × KDP),[19c] Li_2ZrTeO_6 (2.5 × KDP),[19d] and $La_3SnGa_5O_{14}$ (0.4 × $AgGaS_2$)[19e]. However, these mid-IR NLO oxides exhibit smaller SHG responses than extant non-oxides, which may reduce the frequency conversion efficiencies in practical application.

Anionic group theory[20] suggests that the total optical nonlinearity of a crystal is the geometrical superposition of the microscopic second-order susceptibilities (polarization) of the NLO-active anionic groups. Our previous research has demonstrated that quasi-rigid layered structures in π-conjugated oxides offer tremendous possibilities for optical property tuning when appropriate constituents and interatomic connection modes are chosen.[21] In the present study, we propose to create quasi-rigid layered structures by two distinct d^0-TM-centered (d^0-TMO_n) polyhedra that may achieve good mid-IR NLO performance. In contrast to π-conjugated planar anionic units, the incorporation of d^0-TMO_n anionic polyhedra that undergo second-order Jahn−Teller distortions may strengthen the overall SHG response[22] when these d^0-TMO_n polyhedral anions are properly aligned. The creation of quasi-rigid layered structures

from two distinct d^0-TM_n anionic polyhedra,[23] rather than from traditional non-metal oxyanions,[24] could provide a very low-energy optical phonon absorption that would extend the IR absorption edge. In particular, the specific connectivity (e.g. weak interlayer interactions or dangling oxygen atoms between layers) in quasi-rigid layered structures may potentially lead to a reduction in the highest phonon frequency, thereby red-shifting the IR absorption edge.

Herein, we report the successful synthesis of $Cs_4V_8O_{22}$ (CVO), which features honeycomb layers composed of two types of NLO-active units, $[VO_4]$ and $[VO_5]$, with Cs^+ cations located between the layers. The introduction of the $[VO_4]$ and $[VO_5]$ units and the counter cation Cs^+ has several advantages: (i) the distorted $[VO_4]$ and $[VO_5]$ units are conducive to the formation of noncentrosymmetric structures; (ii) a uniform alignment of the distorted $[VO_4]$ and $[VO_5]$ moieties is achieved – this is of crucial importance, as it results in crystal lattice vibrations that optimize the optical phonon modes in the crystal structure; and (iii) the introduction of two types of distorted polyhedra (the $[VO_4]$ and $[VO_5]$ anions) into one molecular structure enhances the SHG response because the polarizations are constructively added. We demonstrate that CVO possesses excellent optical performance, including strong SHG responses (12 × KDP @ 1064 nm; 2.2 × $AgGaS_2$ @ 2100 nm) with phase-matchability, high LIDT (24 × $AgGaS_2$), a wide IR-transparency window, and congruent melting, suggesting that CVO is a promising mid-IR NLO material. The role of the layered structure in CVO in enhancing the SHG response and expanding the transmittance into the IR region has been clarified by first-principles simulations.

Results and Discussion

Crystal Growth and Physicochemical Stability. CVO was synthesized hydrothermally by heating Cs_2CO_3, V_2O_5, $NaBrO_3$ and hydrofluoric acid in deionized water at 210 ºC for 72 h (further details can be found in the Supporting Information). As shown in Figure S1a, millimeter-sized CVO single crystals (the largest one being 2.5 × 1.5 × 1.5 mm^3) have been grown through the hydrothermal technique at 210 °C for 7 days. To understand the solution chemistry of vanadate, the formation regions of the various crystalline phases (obtained through analysis of the reaction products) are denoted in Figure 1 by different colors. The reaction of Cs_2CO_3 with V_2O_5, $NaBrO_3$ and HF at 210 °C in aqueous media for 3 days produces CVO in the form of orange block crystals. $Cs_3V_2O_3F_7$ (CCDC No. 1898810) and α-$CsVO_3$ (CCDC No. 1883612) appear at the upper middle and bottom of the triangle at relatively high temperatures (from 210 °C to 230 °C) and at low temperature (180 °C), respectively. It is noticeable that during the hydrothermal procedure, small amounts of HF are necessary for the synthesis of the $Cs_3V_2O_3F_7$; single crystals of CsV_3O_8[25a] can be isolated at 230 °C without HF. $CsVO_3$, reported by Hawthorne et al.,[25b] predominates in the zone with high cesium concentration and low temperature. No compound was found when a low cesium carbonate content was employed.

As a first step to study the physicochemical stability of CVO, we explored its hygroscopic behavior. Crystals were exposed to air for three months or immersed in water for a week, both at room temperature; the crystals maintained transparency with no decomposition (Figure S1). The thermal stability of CVO was investigated by TGA and DSC (Figure 2a). The TGA curve reveals no obvious weight loss up to 900 °C. The DSC data show a sharp endothermic peak around 456 °C in the heating curve and an exothermic peak around 405 °C in the cooling curve. To further verify the melting process, polycrystalline CVO (500 mg) was placed in a platinum crucible and heated to 500 °C, and then slowly cooled to room temperature. The solidified melt exhibits a diffraction pattern identical to that of the initial CVO powder (Figure 2b). The melting temperature of 456 °C is much lower than that of commercially available IR NLO materials ($AgGaSe_2$, 860 °C; $BaGa_4Se_7$, 968 °C; $AgGaS_2$, 998 °C; $ZnGeP_2$, 1025 °C),[26] as well as the related vanadate Cs_2LiVO_4 (828 °C)[19a]. Our results indicate that CVO melts congruently and so bulk single crystals of CVO may be more easily grown by the Bridgman-Stockbarger technique than from these competitor materials. It should be emphasized that good physicochemical stability is an important prerequisite for mid-IR NLO crystals to be useful in practice.

Crystal Structure of CVO. CVO crystallizes in the orthorhombic crystal system in the polar, noncentrosymmetric space group $Pca2_1$ (crystal class $mm2$, No. 29: see Table S1). As shown in Figures 3b and 3c, its crystal structure is composed of d^0-TM-containing $[V_4O_{11}]_\infty$ anionic layers that stack along the c-axis, while Cs^+ cations occupy the cavities of the neighboring $[V_4O_{11}]_\infty$ layers, serving as interlayer connectors via Cs−O bonds and as counter-ions to maintain the charge balance (Figure 3d). Each honeycomb $[V_4O_{11}]_\infty$ anionic layer consists of the $[VO_4]$ and $[VO_5]$ polyhedra connected via either edge- or corner-shared O atoms in the ab plane (Figures 3a and 3b). The residual apical O atoms of the $[VO_4]$ and $[VO_5]$ polyhedra are almost perpendicular to the $[V_4O_{11}]_\infty$ layer and serve as interlayer bridges.

The asymmetric unit consists of two crystallographically independent Cs atoms, four V atoms, and eleven O atoms. The Cs2 and O7 atoms are located on the two-fold axis. The V atoms adopt two coordination modes, a $[VO_4]$ tetrahedron and a $[VO_5]$ square-based pyramid, with V−O bond lengths in the range 1.602(3)−1.904(2) Å. More detailed crystallographic data for CVO are summarized in Tables S2-S3 of the Supporting Information. The two unique Cs atoms are surrounded by ten or twelve O atoms with Cs−O bond lengths in the range 3.059(2)−3.587(3) Å. The complex Cs-centered $[CsO_{10}]$/$[CsO_{12}]$ polyhedra are further connected with each other, affording a three-dimensional framework (Figure S2).

From the viewpoint of topology, CVO possesses the hcb-type topological layer of $Sr_2Be_2B_2O_7$ (SBBO)[1d], in which the $[BO_3]$ and $[BeO_4]$ units in the honeycomb layers of SBBO are replaced by $[VO_4]$ and $[VO_5]$ polyhedra, optimizing the layered structure. The d^0-TM centered V^{5+} cations adopt four/five-coordination modes and serve as ideal three-connected nodes for SHG activity. In comparison with the layered structure of SBBO (Figure 3e), some distinct differences in the crystallographic architecture of CVO can be seen, which presumably originate from the two different types of NLO-active units. Compared to the $[Be_3B_3O_9]_\infty$ single-layers connected by the Be−O or Sr−O bonds in SBBO, the interlayer bonding for CVO (Cs−O bond) is weaker, resulting in a larger interlayer distance (Figure 3d). The distance between the adjacent quasi-rigid $[V_4O_{11}]_\infty$ single-layers in CVO (5.23 Å) is clearly larger than that of the rigid double layers of SBBO (3.92/3.74 Å) (Figure 3f). This can be attributed to the counter cation Cs^+ with a larger ionic radius and the vertical dangling

oxygen atoms of the [VO_4] and [VO_5] polyhedra. The [VO_4] and [VO_5] polyhedra in the d^0-TM-containing layers of CVO are aligned parallel, in contrast to the [BeO_4] units in the π-conjugated anionic layers which are aligned antiparallel. Simultaneously, an unusual edge-sharing connection arises between two [VO_5] polyhedra that favors the formation of highly condensed layers. Overall, these structural characteristics of the polar CVO, affording a favorable arrangement of the NLO-active units, should be beneficial for achieving a large net macroscopic polarization, close to the maximum possible contribution to the macroscopic SHG response.

SHG Properties. The SHG response as a function of particle size is shown in Figures 4a and 4c; CVO is phase-matchable to both 1064 nm and 2100 nm fundamental radiation. CVO exhibits large SHG responses, 12 × KDP at 1064 nm and 2.2 × $AgGaS_2$ at 2100 nm over the particle size range 105−150 *μ*m (Figures 4b and 4d). Not only are such strong SHG responses sufficient for mid-IR NLO applications, to the best of our knowledge, the SHG efficiency of CVO is the largest of all metal vanadates without additional oxyanions reported to date (Table 1).[27]

The optical properties derive from the structural features of CVO. The dipole moments of the [VO_4] and [VO_5] polyhedra were calculated using the Debye equation,[28] to shed light on the relationship between the functional units and the SHG response, the detailed results for which are summarized in Table S4. Although the net dipole moments of the [VO_4] and [VO_5] polyhedra along the *a*- and *b*-axis directions cancel, their vector sum results in an enhanced net polarization moment down the polar *c*-axis, the major contribution to the total polarization, and the key determinant of the excellent SHG response of CVO.

Optical Properties. The UV-Vis-NIR diffuse reflection spectrum of CVO revealed that the band gap of CVO is ca. 2.72 eV (Figures 4e and S3). This value is significantly larger than that of the commercial IR NLO crystals $AgGaS_2$ (2.52 eV, Figure S3), $ZnGeP_2$ (1.75 eV)[29] and $AgGaSe_2$ (1.8 eV);[29] CVO is therefore expected to exhibit minimal two-photon absorption of common laser radiation and to possess a high LIDT for future practical mid-IR applications. Preliminary measurements of the LIDTs were performed on a powder sample of CVO with $AgGaS_2$ as the reference. The result indicates that CVO exhibits a high LIDT of 51.56 MW/cm^2, about 24 times that of benchmark $AgGaS_2$ (2.1 MW/cm^2) (Table S5).

The IR transmission spectrum of a 1.1 × 1.0 × 0.4 mm^3 single-crystal sample of CVO indicates that the CVO crystal exhibits high transparency in the mid-IR extending to 5.1 *μ*m, and an IR absorption edge at ca. 7.1 *μ*m; the transparency of CVO completely covers the important atmospheric window (3−5 *μ*m). The IR absorption edge of CVO is at a significantly longer wavelength than that of representative NLO oxide materials (e.g. SBBO (3.8 *μ*m),[1d] KTP (4.5 *μ*m)[15]) and comparable to several recently developed mid-IR NLO oxides (e.g. $Rb_4Li_2TiOGe_4O_{12}$ (5.68 *μ*m),[19c] $Li_2K_4TiOGe_4O_{12}$ (5.80 *μ*m),[19b] Li_3VO_4 (LVO, 6.05 *μ*m),[27a] Li_2ZrTeO_6 (7.4 *μ*m)[19d]).

Theoretical Studies. A first-principles simulation[30] was undertaken to calculate the electronic structure and optical properties, and thereby elucidate the origin of the excellent NLO performance at the atomic scale. As displayed in Figure 5a, CVO is a direct-transition semiconductor with a calculated band gap of 2.56 eV, phonon-independent electronic transitions across the forbidden band being beneficial to the generation of a large SHG response. The partial densities of states projected onto the constituent atoms are plotted in Figure 5b. The electronic states below -15 eV are mainly occupied by Cs 5*s* and O 2*s* orbitals, and these are essentially unaffected by external perturbation, contributing little to the optical properties. The Cs 5*p* orbital exhibits a sharp peak at -5.5 eV and hybridizes little with the orbitals of the other atoms, consistent with its strong ionicity. In spite of minor occupation of the conduction band minimum by the Cs 6*p* orbitals, both the top of the valence band (VB, -5−0 eV) and the bottom of the conduction band (CB, 2.56−10 eV) are predominantly occupied by V 3*p* and 3*d* and O 2*p* orbitals. This is consistent with the large SHG response in CVO arising from virtual electronic transitions within the two-dimensional $[V_4O_{11}]_\infty$ layer.

To assess the contribution of the components to the SHG response, real-space atom-cutting and SHG-weighted electron density analysis were performed on CVO. As depicted in Table 2, the contribution of the Cs^+ cations to the SHG response is very small, the $[V_4O_{11}]_\infty$ layers accounting for more than ninety percent of the SHG effect, and with the contribution of [VO_4] similar in magnitude to that of the [VO_5] units. The sign of the contribution of the [VO_4] and [VO_5] units to the SHG coefficient is the same, consistent with the large SHG response arising from the favorable spatial orientation of the two types of units. Almost all of the SHG-weighted electron clouds are located around the $[V_4O_{11}]_\infty$ layers in the virtual electron process, as plotted in Figures 5c and 5d. All of these observations confirm that the $[V_4O_{11}]_\infty$ layer is the principal source of the large SHG response in CVO.

The IR absorption edge of CVO (7.1 *μ*m) is red-shifted in comparison with those of established metal vanadates (e.g. 6.05 *μ*m for LVO). It is clearly desirable to understand the microscopic mechanism of the good optical transmittance properties. Optical transmittance in the IR region is closely related to the interactions between the lattice phonons and the external photons, so the phonon spectrum should provide insight into the reason(s) for the wide transmittance in the IR region. There are no imaginary frequencies in the phonon spectrum of CVO (Figure S4), confirming its dynamic stability. A calculation of the phonon density of states of CVO was carried out and a similar calculation was performed on LVO for comparison (Figure 6). Unlike LVO, phonons in the high-frequency range undergo a significant shift to the low-frequency range, which can be attributed to the quasi-rigid layers resulting from the interaction of the [VO_4] and [VO_5] groups in CVO.,External photons therefore interact with reduced phonon numbers in the high-frequency range, and are consequently less effectively absorbed, resulting in the red-shifted in IR absorption edge of CVO. In contrast, in LVO all eigenstates in the high-frequency range are occupied by large numbers of phonons and can interact with the external photons, and so the IR absorption edge coincides with the highest lattice vibration frequency. The two-dimensional layer architecture therefore prohibits V−O vibrations at room temperature, and removes the interactions of the high-frequency phonons, resulting in the observed red-shifted IR absorption edge.

Conclusion

In summary, we have designed and successfully synthesized a vanadate crystal CVO, which features a honeycomb layered structure consisting of ordered [VO_4] and [VO_5] polyhedra, with

Cs^+ cations located between the layers. CVO exhibits optimized optical properties required for mid-IR NLO applications, including a wide IR transparency window, the strongest SHG response (12 × KDP @ 1064 nm; 2.2 × $AgGaS_2$ @ 2100 nm) among metal vanadates without additional oxyanions, a high LIDT (24 × $AgGaS_2$), phase-matchability, congruent-melting behavior and physicochemical stability. First-principles calculations suggest that the strong SHG responses can be ascribed to the additively ordered alignment of the $[VO_4]$ and $[VO_5]$ units within the $[V_4O_{11}]_\infty$ layer, while the expanded IR absorption edge can be attributed to the special lattice vibration characteristics that result from the optimized layered structure. The design strategy for creating quasi-rigid layered structures with two distinct d^0-TMO_n anionic polyhedra may afford a reliable and versatile structure-driven approach to novel optoelectronic functional materials.

Acknowledgements

This research was financially supported by the National Natural Science Foundation of China (Nos. 51432006 and 52002276), the Ministry of Education of China for the Changjiang Innovation Research Team (No. IRT14R23), and the Ministry of Education and the State Administration of Foreign Experts Affairs for the 111 Project (No. B13025). M.G.H. thank the Australian Research Council for support (DP170100411).

Keywords: nonlinear optics • mid-infrared • density functional calculations • second-harmonic generation • vanadates

[1] a) D. Cyranoski, *Nature* **2009**, *457*, 953-955; b) P. S. Halasyamani, K. R. Poeppelmeier, *Chem. Mater.* **1998**, *10*, 2753-2769; c) N. Savage, *Nat. Photonics* **2007**, *1*, 83-85; d) C. T. Chen, Y. B. Wang, B. C. Wu, K. C. Wu, W. L. Zeng, L. H. Yu, *Nature*, **1995**, *373*, 322-324.

[2] a) H. W. Yu, M. L. Nisbet, K. R. Poeppelmeier, *J. Am. Chem. Soc.* **2018**, *140*, 8868-8876; b) H. W. Yu, W. G. Zhang, J. Young, J. M. Rondinelli, P. S. Halasyamani, *Adv. Mater.* **2015**, *27*, 7380-7385; c) H. M. Zhou, L. Xiong, L. Chen, L. M. Wu, *Angew. Chem.* **2019**, *131*, 10084-10088; *Angew. Chem. Int. Ed.* **2019**, *58*, 9979-9983; d) F. F. Mao, C. L. Hu, X. Xu, D. Yan, B. P. Yang, J. G. Mao, *Angew. Chem.* **2017**, *129*, 2183-2187; *Angew. Chem. Int. Ed.* **2017**, *56*, 2151-2155. e) C. Wu, T. H. Wu, X. X. Jiang, Z. J. Wang, H. Y. Sha, L. Lin, Z. S. Lin, Z. P. Huang, X. F. Long, M. G. Humphrey, C. Zhang, *J. Am. Chem. Soc.* **2021**, *143*, 4138-4142.

[3] a) C. T. Chen, B. C. Wu, A. D. Jiang, G. M. You, *Sci. Sin., Ser. B* **1985**, *28*, 235-243; b) C. T. Chen, Y. C. Wu, A. D. Jiang, B. C. Wu, G. M. You, R. K. Li, S. J. Lin, *J. Opt. Soc. Am. B* **1989**, *6*, 616-621; c) Y. C. Wu, T. Sasaki, N. Nakai, A. Yokotani, H. G. Tang, C. T. Chen, *Appl. Phys. Lett.* **1993**, *62*, 2614-2615; d) J. J. De Yoreo, A. K. Burnham, P. K. Whitman, *Int. Mater. Rev.* **2002**, *47*, 113-152.

[4] F. Liang, L. Kang, Z. S. Lin, Y. C. Wu, *Cryst. Growth Des.* **2017**, *17*, 2254-2289.

[5] a) B. Tell, H. M. Kasper, *Phys. Rev. B* **1971**, *4*, 4455-4459; b) U. Simon, Z. Benko, M. W. Sigrist, R. F. Curl, F. K. Tittel, *Appl. Opt.* **1993**, *32*, 6650-6655; c) G. D. Boyd, E. Buehler, F. G. Storz, *Appl. Phys. Lett.* **1971**, *18*, 301-304.

[6] a) T. K. Bera, J. I. Jang, J. H. Song, C. D. Malliakas, A. J. Freeman, J. B. Ketterson, M. G. Kanatzidis, *J. Am. Chem. Soc.* **2010**, *132*, 3484-3495; b) B. W. Liu, X. M. Jiang, H. Y. Zeng, G. C. Guo, *J. Am. Chem. Soc.* **2020**, *142*, 10641-10645; c) H. Lin, L. Chen, L. J. Zhou, L. M. Wu, *J. Am. Chem. Soc.* **2013**, *135*, 12914-12921; d) C. Yang, X. Liu, C. Teng, X. Cheng, F. Liang, Q. Wu, *Mater. Today Phys.* **2001**, *19*, 100432; e) X. L. Chen, Q. Jing, K. M. Ok, *Angew. Chem.* **2020**, *132*, 20503-20507; *Angew. Chem. Int. Ed.* **2020**, *59*, 20323-20327; f) J. D. Chen, C. S. Lin, D. Zhao, M. Luo, G. Peng, B. X. Li, S. D. Yang, Y. S. Sun, N. Ye, *Angew. Chem.* **2020**, *132*, 23755-23759; *Angew. Chem. Int. Ed.* **2020**, *59*, 23549-23553.

[7] a) I. Chung, M. G. Kanatzidis, *Chem. Mater.* **2014**, *26*, 849-869; b) A. Schliesser, N. Picque, T. W. Haensch, *Nat. Photonics* **2012**, *6*, 440-449.

[8] a) K. Wu, Z. H. Yang, S. L. Pan, *Angew. Chem.* **2016**, *128*, 6825-6827; *Angew. Chem. Int. Ed.* **2016**, *55*, 6713-6715; b) S. P. Guo, Y. Chi, G. C. Guo, *Coord. Chem. Rev.* **2017**, *335*, 44-57.

[9] a) K. M. Ok, *Acc. Chem. Res.* **2016**, *49*, 2774-2785; b) D. Vitzthum, K. Wurst, J. M. Pann, P. Bruggeller, M. Seibald, H. Huppertz, *Angew. Chem.* **2018**, *130*, 11622-11626; *Angew. Chem. Int. Ed.* **2018**, *57*, 11451-11455; c) J. Chen, C. L. Hu, F. F. Mao, B. P. Yang, X. H. Zhang, J. G. Mao; *Angew. Chem.* **2019**, *131*, 11792-11795; *Angew. Chem. Int. Ed.* **2019**, *58*, 11666-11669; d) H. W. Yu, J. Young, H. P. Wu, W. G. Zhang, J. M. Rondinelli, P. S. Halasyamani, *J. Am. Chem. Soc.* **2016**, *138*, 4984-4989; e) R. L. Tang, C. L. Hu, B. L. Wu, Z. Fang, Y. Chen, J. G. Mao, *Angew. Chem.* **2019**, *131*, 15502-15505; *Angew. Chem. Int. Ed.* **2019**, *58*,15358-15361; (f) G. Peng, N. Ye, Z. S. Lin, L. Kang, S. L. Pan, M. Zhang, C. S. Lin, X. F. Long, M. Luo, Y. Chen, Y. H. Tang, F. Xu, T. Yan, *Angew. Chem.* **2018**, *130*, 9106-9110; *Angew. Chem. Int. Ed.* **2018**, *57*, 8968-8972.

[10] a) X. S. Lin, G. Zhang, N. Ye, *Cryst. Growth Des.* **2009**, *9*, 1186-1189; b) X. L. Chen, H. Jo, K. M. Ok, *Angew. Chem.* **2020**, *132*, 7584-7590; *Angew. Chem. Int. Ed.* **2020**, *59*, 7514-7520; c) S. P. Guo, Y. Chi, H. G. Xue, *Angew. Chem.* **2018**, *130*, 11714-11717; *Angew. Chem. Int. Ed.* **2018**, *57*, 11540-11543; c) C. Li, W. L. Yin, P. F. Gong, X. S. Li, M. L. Zhou, A. Mar, Z. S. Lin, J. Y. Yao, Y. C. Wu, C. T. Chen, *J. Am. Chem. Soc.* **2016**, *138*, 6135-6138; e) H. Lin, W. B. Wei, H. Chen, X. T. Wu, Q. L. Zhu, *Coord. Chem. Rev.* **2020**, *406*, 213150.

[11] a) M. Mutailipu, K. R. Poeppelmeier, S. L. Pan, *Chem. Rev.* **2021**, *121*, 1130−1202; b) S. G. Zhao, L. Kang, Y. G. Shen, X. D. Wang, M. A.Asghar, Z. S. Lin, Y. Y. Xu, S. Y. Zeng, M. C. Hong, J. H. Luo, *J. Am. Chem. Soc.* **2016**, *138*, 2961-2964.

[12] a) X. M. Liu, P. F. Gong, Y. Yang, G. M. Song, Z. S. Lin, *Coord. Chem. Rev.* **2019**, *400*, 213045; b) Y. X. Song, M. Luo, C. S. Lin, N. Ye, *Chem. Mater.* **2017**, *29*, 896-903.

[13] T. T. Tran, J. Young, J. M. Rondinelli, P. S. Halasyamani, *J. Am. Chem. Soc.* **2017**, *139*, 1285-1295; G. H. Zou, N. Ye, L. Huang, X. Lin, *J. Am. Chem. Soc.*, **2011**, *133*, 20001-20007.

[14] a) P. Yu, L. M. Wu, L. J. Zhou, L. Chen, *J. Am. Chem. Soc.* **2014**, *136*, 480-487; b) C. Wu, X. X. Jiang, Z. J. Wang, H. Y. Sha, Z. S. Lin, Z. P. Huang, X. F. Long, M. G. Humphrey, C. Zhang, *Angew. Chem.* **2021**, *133*, 14932-14936; *Angew. Chem. Int. Ed.* **2021**, *60*, 14806-14810.

[15] P. Becker, *Adv. Mater.* **1998**, *10*, 979-992.

[16] H. Zhang, M. Zhang, S. L. Pan, X. Y. Dong, Z. H. Yang, X. L. Hou, Z. Wang, K. B. Chang, K. R. Poeppelmeier, *J. Am. Chem. Soc.* **2015**, *137*, 8360-8363.

[17] a) E. O. Chi, K. M. Ok, Y. Porter, P. S. Halasyamani, *Chem. Mater.* **2006**, *18*, 2070-2074; b) L. Lin, X. X. Jiang, C. Wu, L. H. Li, Z. S. Lin, Z. P. Huang, M. G. Humphrey, C. Zhang, *ACS Appl. Mater. Interfaces* **2020**, *12*, 49812-49821.

[18] a) Y. L. Deng, L. Huang, X. H. Dong, L. Wang, K. M. Ok, H. M. Zeng, Z. E. Lin, G. H. Zou, *Angew. Chem.* **2020**, *132*, 21337-21342; *Angew. Chem. Int. Ed.* **2020**, *59*, 21151-21156; b) F. G. You, F. Liang, Q. Huang, Z. G. Hu, Y.C. Wu, Z. S. Lin, *J. Am. Chem. Soc.* **2019**, *141*, 748-752.

[19] a) G. P. Han, Y. Wang, X. Su, Z. H. Yang, S. L. Pan, *Sci. Rep.* **2017**, *7*, 1901; b) J. Xu, H. P. Wu, H. W. Yu, W. G. Zhang, Z. G. Hu, J. Wang, Y. C. Wu, P. S. Halasyamani, *Chem. Mater.* **2020**, *32*, 906-912; c) M. J. Xia, C. Tang, R. K. Li, *Angew. Chem.* **2019**, *131*, 18425-18428; *Angew. Chem. Int. Ed.* **2019**, *58*, 18257-18260; d) W. Q. Lu, Z. L. Gao, X. T. Liu, X. X. Tian, Q. Wu, C. G. Li, Y. X. Sun, Y. Liu, X. T. Tao, *J. Am. Chem. Soc.* **2018**, *140*, 13089-13096; e) H. C. Lan, F. Liang, X. X. Jiang, C. Zhang, H. H. Yu, Z. S. Lin, H. J. Zhang, J. Y. Wang, Y. C. Wu, *J. Am. Chem. Soc.* **2018**, *140*, 4684-4690.

[20] C. T. Chen, *Sci. Sin.* **1979**, *22*, 756-776.

[21] a) C. Wu, G. Yang, M. G. Humphrey, C. Zhang, *Coord. Chem. Rev.* **2018**, *375*, 459-488; b) C. Wu, X. X. Jiang, Z. J. Wang, L. Lin, Z. S. Lin, Z. P. Huang, X. F. Long, M. G. Humphrey, C. Zhang, *Angew. Chem. Int. Ed.* **2021**, *60*, 3464-3468; *Angew. Chem.* **2021**, *133*, 3506-3510.

[22] H. S. Ra, K. M. Ok, P. S. Halasyamani, *J. Am. Chem. Soc.* **2003**, *125*, 7764-7765

[23] C. Wu, L. Lin, X. X. Jiang, Z. S. Lin, Z. P. Huang, M. G. Humphrey, P. S. Halasyamani, C. Zhang, *Chem. Mater.* **2019**, *31*, 10100-10108.

[24] X. F. Wang, Y. Wang, B. B. Zhang, F. F. Zhang, Z. H. Yang, S. L. Pan, *Angew. Chem.* **2017**, *129*, 14307-14311; *Angew. Chem. Int. Ed.* **2017**, *56*, 14119-14123.

[25] a) H. T. Evans, S. Block, *Inorg. Chem.* **1966**, *5*, 1808-1814; b) F. C. Hawthorne, C. Calvo, *J. Solid State Chem.* **1977**, *22*, 157-170.

[26] Z. Li, X. X. Jiang, C. J. Yi, M. L. Zhou, Y. W. Guo, X. Y. Luo, Z. S. Lin, Y. C. Wu, Y. G. Shi, J. Y. Yao, *J. Mater. Chem. C* **2018**, *6*, 10042-10049.

[27] a) Z. H. Chen, Z. Z. Zhang, X. Y. Dong, Y. J. Shi, Y. Q. Liu, Q. Jing, *Cryst. Growth Des.* **2017**, *17*, 2792-2800; b) J. Yeon, S. H. Kim, P. S. Halasyamani, *Inorg. Chem.* **2010**, *49*, 6986-6993; c) W. Q. Chen, W. Y. Zhang, M. H. Lee, Q. Jing, X. F. Lu, Z. H. Chen, *Opt. Mater.* **2019**, *88*, 642-647; d) M. Bosacka, *Mater. Res. Bull.* **2009**, *44*, 2252-2254; e) Z. B. Lin, G. F. Wang, L. Z. Zhang, *J. Cryst. Growth* **2007**, *304*, 233-235; f) A. K. Paidi, P. W. Jaschin, K. B. R. Varma, K. Vidyasagar, *Inorg. Chem.* **2017**, *56*, 12631-12640; g) H. Y. Chang, S. H. Kim, K. M. Ok, P. S. Halasyamani, *Chem. Mater.* **2009**, *21*, 1654-1662.

[28] P. A. Maggard, T. S. Nault, C. L. Stern, K. R. Poeppelmeier, *J. Solid State Chem.* **2003**, *175*, 27-33.

[29] D. N. Nikogosyan, *Nonlinear Optical Crystals: A Complete Survey*, Springer, Heidelberg, **2012**.

[30] a) S. J. Clark, M. D. Segall, C. J. Pickard, P. J. Hasnip, M. J. Probert, K. Refson, M. C. Payne, *Z. Kristallogr.* **2005**, *220*, 567-570; b) W. Kohn, L. J. Sham, *Phys. Rev.* **1965**, *140*, 1133-1138.

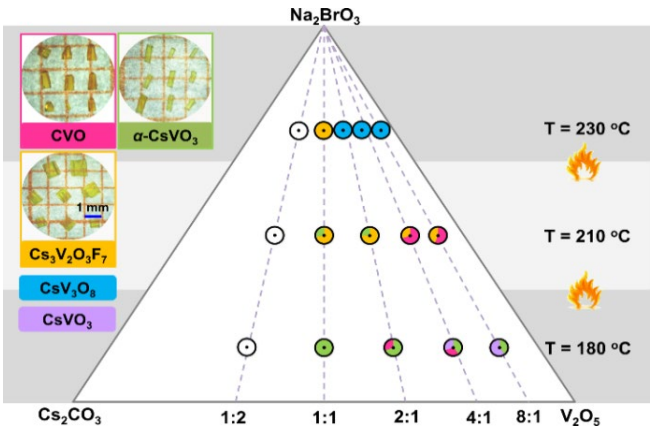

Figure 1. Experimental solid phase space of the Cs_2CO_3-V_2O_5-$NaBrO_3$-HF system with the temperature zones shown in the background in gray. The compositions of the various phases synthesized in each experimental point are shown by circles of different colors. The phases of $CsVO_3$ and CsV_3O_8 reported in reference 25 were reproduced in our experiments through hydrothermal methods.

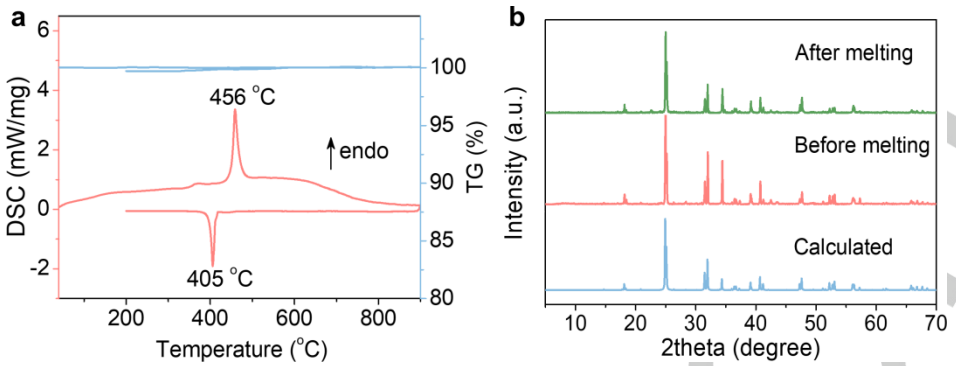

Figure 2. (a) Thermogravimetric and differential scanning calorimetry (DSC) curves for CVO. "Endo" indicates the endothermic direction. (b) Calculated and experimental PXRD for CVO.

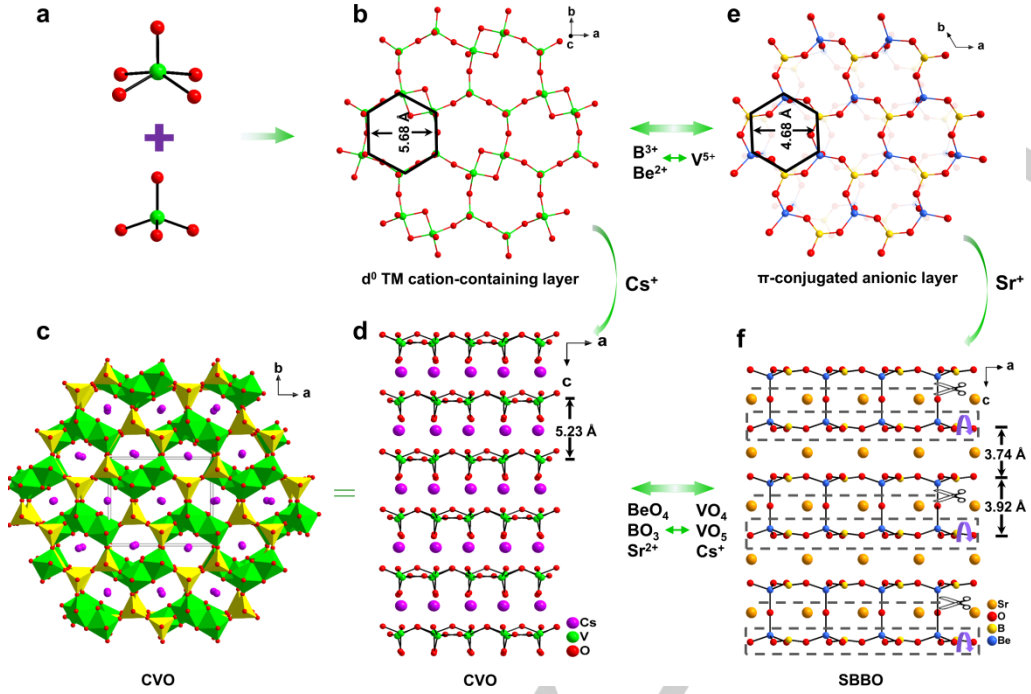

Figure 3. The VO_5 and VO_4 units (a). View of the d^0-TM-containing layer in CVO in the *ab* plane (b). Perspective view of CVO along the *c*-axis (c). Perspective view of the π-conjugated anionic layer in SBBO (e). Structural comparison of CVO (d) and SBBO (f) along the *b*-axis.

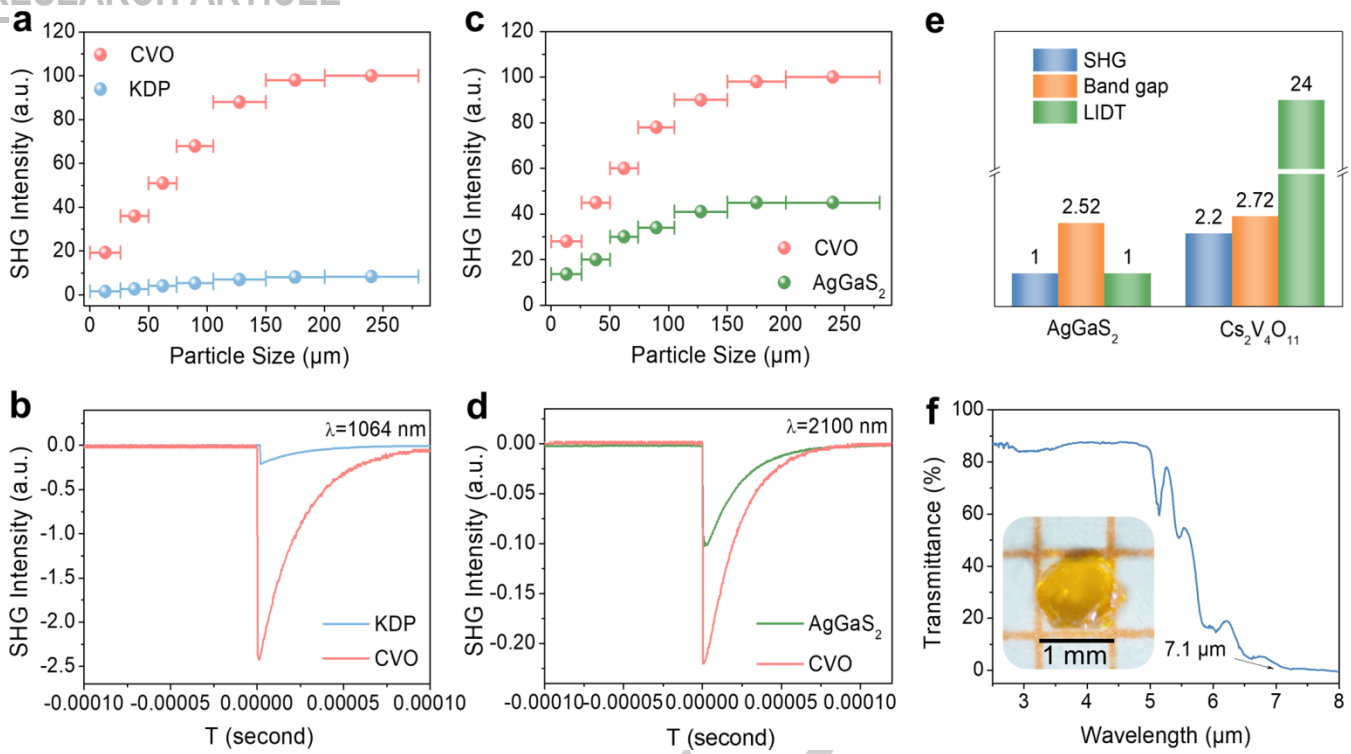

Figure 4. Measured SHG intensity versus CVO particle size with 1064 nm (a) and 2100 nm (c) laser radiation. Oscilloscope traces of the SHG signals (105−150 μm) are shown in (b) and (d). KDP and $AgGaS_2$ were used as references for the SHG measurements at 1064 and 2100 nm, respectively. (e) Experimental band gaps and relative SHG and LIDT intensities of CVO and $AgGaS_2$. (f) IR transmission spectrum of the CVO single crystal (Inset: crystal photo).

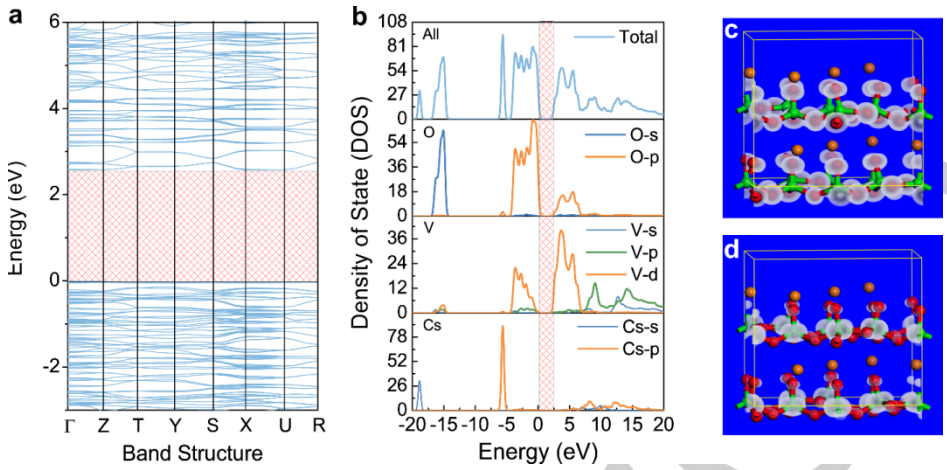

Figure 5. (a) Electronic band structure. (b) Total density of states and partial density of states projected onto the orbitals of the constituent atoms. SHG weighted electron clouds for (c) occupied and (d) unoccupied orbitals in the virtual electron process.

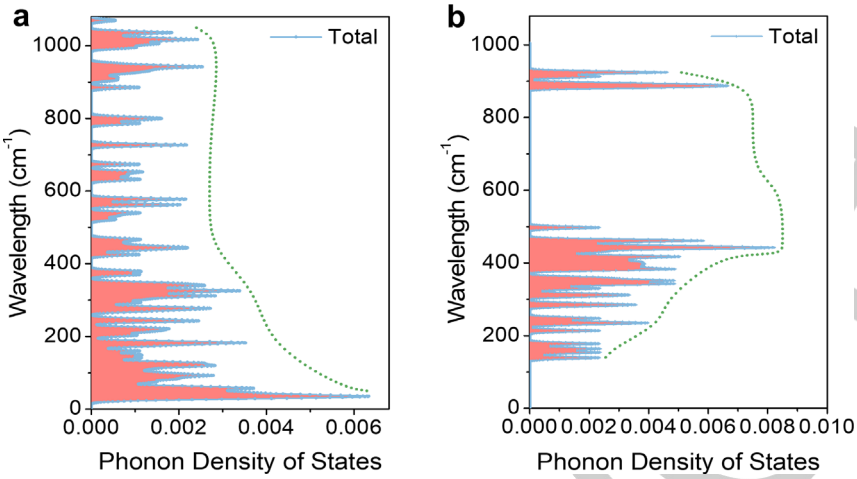

Figure 6. Phonon density of states for CVO (a) and LVO (b). The green dotted curves are drawn to guide the eyes and are not fits to the data.

Table 1. Comparison of the SHG responses of noncentrosymmetric metal vanadates at 1064 nm.

Compound	Space group	PM/NPM	SHG response (× KDP)
$K_3V_5O_{14}$[27b]	*P*31*m*	PM	3.25
$Rb_3V_5O_{14}$[27b]	*P*31*m*	PM	2
$Tl_3V_5O_{14}$[27b]	*P*31*m*	PM	2.5
$BaV_2O_6{\cdot}H_2O$[27c]	$P2_12_12_1$	NPM	0.5
Li_3VO_4[27a]	$Pmn2_1$	PM	9.5
Cd_2InVO_6[27d]	$P3_1$	PM	1.75
$YCa_9(VO_4)_7$[27e]	*R*3	PM	4.7
$SrNb_2V_2O_{11}$[27f]	*Cm*	PM	4.4
$SrTa_2V_2O_{11}$[27f]	*Cm*	PM	5.5
$RbSe_2V_3O_{12}$[27g]	$P6_3$	NPM	1
$TlSe_2V_3O_{12}$[27g]	$P6_3$	NPM	1.25
Rb_2LiVO_4[19a]	$Cmc2_1$	PM	4
Cs_2LiVO_4[19a]	$Cmc2_1$	PM	5
CVO (this work)	$Pca2_1$	PM	12

Table 2. Real-space atom-cutting analysis of CVO[a].

	d_{31}	d_{32}	d_{33}
total	-14.9	-15.1	14.6
Cs	0.4	-0.7	0.8
$[V_4O_{11}]$	-13.2	-14.6	13.7
$[VO_4]$	-8.3	-9.4	9.7
$[VO_5]$	-7.7	-8.6	6.4

[a] d values in pm/V.

Entry for the Table of Contents

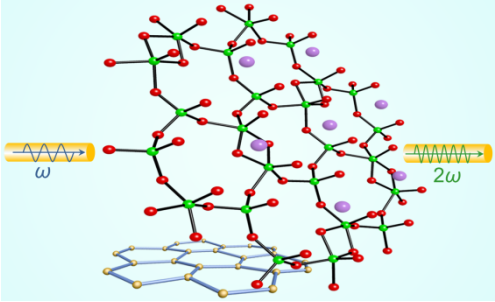

Access to the elusive mid-infrared by direct second-harmonic generation (SHG) enabled by a vanadate crystal is reported. $Cs_4V_8O_{22}$ exhibits a wide transparent range, a strong SHG response, a large laser damage threshold and congruent-melting behavior. Quantum mechanical calculations demonstrate the key role played by its quasi-rigid layered structure in the improvement in linear and second-order nonlinear optical performance.